---

**Article:**
Chen, L. and de Borst, R. orcid.org/0000-0002-3457-3574 (2022) Phase-field regularised cohesive zone model for interface modelling. Theoretical and Applied Fracture Mechanics, 122. 103630. ISSN 0167-8442

https://doi.org/10.1016/j.tafmec.2022.103630

---

Theoretical and Applied Fracture Mechanics 122 (2022) 103630

Contents lists available at ScienceDirect

Theoretical and Applied Fracture Mechanics

journal homepage: www.elsevier.com/locate/tafmec

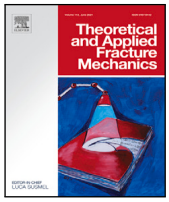

# Phase-field regularised cohesive zone model for interface modelling

L. Chen [a], R. de Borst [b,*]

[a] Northeastern University, Key Laboratory of Ministry of Education on Safe Mining of Deep Metal Mines, Shenyang 110819, China
[b] University of Sheffield, Department of Civil and Structural Engineering, Sheffield S1 3JD, UK

ARTICLE INFO

*Keywords:*
Interface
Cohesive zone model
Phase field model
Fracture
Damage

ABSTRACT

A discrete interface is represented as a smeared interface in the framework of phase field regularisation. Due to the numerical challenge when imposing boundary conditions we prescribe the phase field in the domain using analytical solutions. We obtain the displacement and the strain from the variational form of the energy functional, but also in the framework of the regularised extended finite element method. Indeed, both approaches result in identical forms, validating the rigour of the method. We have examined different forms of the phase field model and conclude that models with a compact support are more appropriate for modelling interfaces. The method combines advantages of discrete and smeared approaches. Compared to discrete interface models, the method holds similar properties as the extended finite element method (XFEM): no need to treat cracks as geometric discontinuities and avoiding mesh refinement around crack tips. Different from the XFEM, however, the method does not introduce enrichment functions to describe cracks. An advantage compared to the phase field method is that this method directly employs the cohesive zone law from the discrete model, which is physically relevant. The accuracy of the approach for cohesive interface modelling is demonstrated by several numerical examples, including a bar, an L-shaped specimen, and a fibre embedded in an epoxy matrix.

## 1. Introduction

Material or structural design often needs multi-components at the material level or at the structural level. Invariably, the interface is the location for material or structural failure, and thus plays a major role on the material properties of materials or structures. An accurate modelling of interface failure is therefore crucial for the prediction of the strength of the final product. The numerical simulation of interface failure is a scientifically challenging issue. Starting from the early simulations in the 1960s [1,2], two different approaches have been pursued for modelling fracture: discrete and smeared models [3]. The discrete model treats the interface as a geometric discontinuities, leading to topological changes [1], while the smeared approach distributes discontinuities over a small, but finite band (with concomitant high local strains), e.g. [2]. Later, the smeared approach has been casted in a damage format, e.g. [4], and more recently, phase-field models were introduced to describe brittle fracture in an elegant manner [5–8].

The phase field model describes the crack by a scalar phase field variable, and is appropriate for the simulation of complex crack patterns [9,10]. The vast majority of phase-field models have been applied to the analysis of brittle fracture, e.g. [9]. However, their extension to the cohesive fracture is underdeveloped. Verhoosel and de Borst [11] proposed a cohesive phase field model, employing an auxiliary field to model the displacement jump, required as an input in a cohesive-zone model, see also [12–14]. Nguyen et al. [15] avoided an auxiliary field by computing the displacement jump at two points near the interface. However, the choice of the location of these points is rather arbitrary and definitely problem-dependent. Another approach to model the cohesive fracture is the phase-field regularised cohesive-zone model. It modifies the degradation function and the homogeneous energy dissipation function [16–18]. The surface energy functional is the same as that for brittle fracture, while the cohesive zone law is reproduced in a one-dimensional setting. In an attempt to compute the displacement jump Chukwudozie et al. [19] employed an integration approach within the context of the analysis of hydraulic fracturing in porous media and Yoshioka et al. [20] used the integration approach in different settings.

The cohesive phase field model of Verhoosel and de Borst [11] uses an independent interpolation for the displacement jump. It is an elegant and, in principle, powerful approach to implement the cohesive interface within the context of phase field modelling. The model is a combination of discrete and smeared approaches. It utilises the regularised Dirac-delta function from the phase field model, and transfers the discrete interface into a smeared one. To describe the

* Corresponding author.
*E-mail address:* r.deborst@sheffield.ac.uk (R. de Borst).

https://doi.org/10.1016/j.tafmec.2022.103630
Received 31 July 2022; Received in revised form 26 August 2022; Accepted 10 October 2022
Available online 18 October 2022

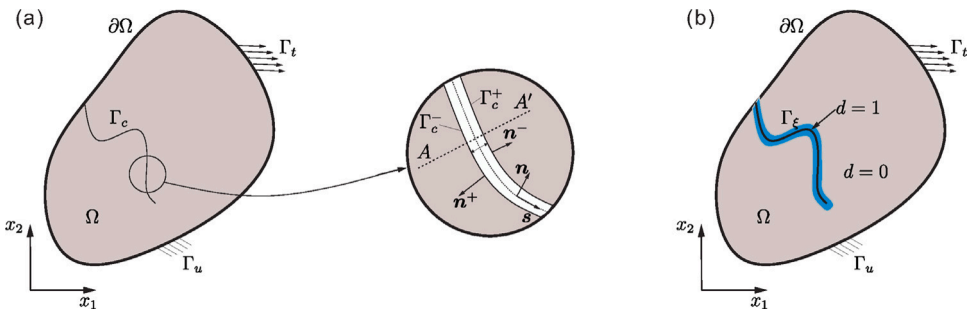


**Fig. 1.** (a) a solid body $\boldsymbol{\Omega}$ with a discrete interface $\Gamma_c$. $\Gamma_c$ is an interface boundary with positive and negative sides, $\Gamma_c^+$ and $\Gamma_c^-$, respectively. Boundary $\Gamma_u$ is prescribed with a displacement $\bar{\mathbf{u}}$; $\Gamma_t$ with a prescribed traction $\bar{\mathbf{t}}$; (b) a solid body $\boldsymbol{\Omega}$ with a smeared interface $\Gamma_\xi$ (blue area).

interface behaviour, the cohesive zone law from the discrete model is directly used. This method combines advantages of discrete and smeared approaches. The interface is represented in a distributed sense, so there is no need of topological changes, similar to the extended finite element method (XFEM). Different from the XFEM it is unnecessary to introduce enrichment functions to describe an interface. The use of the cohesive zone law from the discrete model is directly based on the physics, and different from the modification of the degradation function in the phase-field model [17]. Any form of the cohesive zone law can be incorporated in the method, while in the phase-field model [17] only a specific form of the cohesive zone law could so far be included. Indeed, only the exponential form of the phase field model [7] has been considered [11–14]. The support of the exponential function is spread over the entire domain, thus violating the localisation property of the interface. Moreover, the relation of the method to the discrete model is not elaborated rigorously in a mathematical sense. Also, the issue of how to implement prescribing the displacement jump degrees of freedom will be addressed herein.

This study will address the general case of a phase-field regularised interface cohesive-zone model, and deal with different forms of phase field function. We will focus on the imposition of the phase field variable in the domain, the localised property of the model, and prescribing the jump degrees of freedom. The link between the model and the extended finite element method will also be discussed. We will start this contribution with a concise description of regularised cohesive zone models and phase-field representations of cohesive interfaces. Subsequently, the governing equations are given. The finite element implementation of the model is discussed in Section 5. Finally, numerical examples are presented to validate the approach and conclusions are drawn.

## 2. Regularised cohesive zone model

Introduced in [21,22], cohesive zone model is now widely employed to model fracture [23,24]. It essentially relates tractions on an interface in a solid body to the displacement jump along the interface. In the model an interface $\Gamma_c$ is placed in the physical domain $\Omega$ with positive and negative sides, $\Gamma_c^+$ and $\Gamma_c^-$ respectively, as illustrated in Fig. 1(a). In this contribution the interface $\Gamma_c$ is assumed to be pre-defined, as is the case of delamination of composite structures, for instance. Infinitesimal strains and linear elastic material behaviour have been assumed.

In the discrete cohesive fracture model, the potential energy is given as:

$$\Psi_{\text{pot}} = \int_\Omega \psi^e\left(\boldsymbol{\varepsilon}\left(\mathbf{u}\right)\right) \mathrm{d}V + \int_\Gamma \mathcal{G}\left(\llbracket \mathbf{u} \rrbracket, \boldsymbol{\kappa}\right) \mathrm{d}A \tag{1}$$

with $\boldsymbol{\kappa}$ being a history parameter, obeying the Kuhn–Tucker conditions to distinguish between loading and unloading.

Obviously, one can include failure in the bulk by introducing the surface energy function $\int_\Gamma \mathcal{G}_c \mathrm{d}A$ ($\mathcal{G}_c$ fracture toughness), for instance [15,25–27]. In such a scenario, the combination of cohesive cracking for the interface and subsequent kinking of the primary crack into the bulk can be considered. In the current study, the focus is on the phase field representation of the interface, the incorporation of the cohesive zone law in the phase field framework, and the proof that the current method and the extended finite element method are identical in format. Extension to the bulk and combination with cohesive cracking in the interface will be a subject of future studies.

$\psi^e$ represents the elastic energy density, given by Hooke's law for an isotropic linear elastic material:

$$\psi^e = \frac{1}{2}\lambda\varepsilon_{ii}\varepsilon_{jj} + \mu\varepsilon_{ij}\varepsilon_{ij} \tag{2}$$

with $\lambda$ and $\mu$ being Lamé constants. $\boldsymbol{\varepsilon}$ is the infinitesimal strain tensor, with components:

$$\varepsilon_{ij} = u_{(i,j)} = \frac{1}{2}\left(\frac{\partial u_i}{\partial x_j} + \frac{\partial u_j}{\partial x_i}\right) \tag{3}$$

where $\mathbf{u}$ is the displacement field, while $\llbracket \mathbf{u} \rrbracket$ denotes the displacement jump across the interface $\Gamma_c$, expressed as

$$\llbracket \mathbf{u} \rrbracket = \mathbf{u}^+ - \mathbf{u}^- \qquad \text{on} \qquad \Gamma_c \tag{4}$$

with $\mathbf{u}^+$ and $\mathbf{u}^-$ being the displacement on the positive and negative sides, $\Gamma_c^+$ and $\Gamma_c^-$ respectively. In Eq. (1), $\mathcal{G}(\llbracket \mathbf{u} \rrbracket, \boldsymbol{\kappa})$ is the fracture energy function, representing the energy dissipation upon the creation of a unit crack surface. This energy is released gradually in cohesive zone models, depending on the displacement jump function $\llbracket \mathbf{u} \rrbracket$ and the history parameter $\boldsymbol{\kappa}$.

The cohesive tractions are obtained by differentiating the fracture energy with respect to the displacement jump:

$$\mathbf{t}\left(\llbracket \mathbf{u} \rrbracket, \boldsymbol{\kappa}\right) = \frac{\partial \mathcal{G}\left(\llbracket \mathbf{u} \rrbracket, \boldsymbol{\kappa}\right)}{\partial \llbracket \mathbf{u} \rrbracket} \tag{5}$$

where $\mathbf{t}\left(\llbracket \mathbf{u} \rrbracket, \boldsymbol{\kappa}\right)$ and $\llbracket \mathbf{u} \rrbracket$ are given in the global coordinate system $\left(x_1, x_2\right)$. In cohesive zone models, tractions $\mathbf{t}$ are explicitly linked with the displacement jump $\llbracket \mathbf{u} \rrbracket$. Different types of cohesive zone laws are available in the literature [28], such as the Xu–Needleman law, the bilinear law, etc. We can straightforwardly incorporate these cohesive zone laws in the method.

In this study, the Xu–Needleman law is used [23], defining the traction in the normal and shear directions as:

$$\begin{aligned} t_n &= \frac{\mathcal{G}_c}{\delta_n}\frac{\llbracket v_n \rrbracket}{\delta_n}\exp\left(-\frac{\llbracket v_n \rrbracket}{\delta_n}\right)\exp\left(-\frac{\llbracket v_s \rrbracket^2}{\delta_s^2}\right) \\ t_s &= \frac{2\mathcal{G}_c}{\delta_s}\frac{\llbracket v_s \rrbracket}{\delta_s}\left(1+\frac{\llbracket v_n \rrbracket}{\delta_n}\right)\exp\left(-\frac{\llbracket v_n \rrbracket}{\delta_n}\right)\exp\left(-\frac{\llbracket v_s \rrbracket^2}{\delta_s^2}\right), \end{aligned} \tag{6}$$

which relates to tractions $\mathbf{t}$ in Eq. (5) and the displacement jump in Eq. (4) via a standard transformation:

$$\begin{aligned} \mathbf{t} \quad &= \mathbf{R}^T\mathbf{t}_d = \mathbf{R}^T\left[t_s \;\; t_n\right]^T, \\ \llbracket \boldsymbol{v} \rrbracket \;&= \left[\llbracket v_s \rrbracket \;\; \llbracket v_n \rrbracket\right]^T = \mathbf{R}\llbracket \mathbf{u} \rrbracket = \mathbf{R}\left[\llbracket u_{x_1} \rrbracket \;\; \llbracket u_{x_2} \rrbracket\right]^T \end{aligned} \tag{7}$$

in which $\delta_n$ and $\delta_s$ are the characteristic length parameters defined by $\delta_n = \mathcal{G}_c/\left(t_u e\right)$ and $\delta_s = \mathcal{G}_c\Big/\left(t_u\sqrt{\frac{1}{2}}e\right)$ with $e = \exp\left(1\right)$; $t_u$ and

$\mathcal{G}_c$ represent the fracture strength and fracture toughness, respectively; $[\![v_n]\!]$ and $[\![v_s]\!]$ are the displacement jump in the normal and shear direction, separately; $\mathbf{R}$ denotes a rotation matrix [29]. To prevent interpenetration, a penalty stiffness $k_p$ is specified in the normal direction of the interface $\Gamma_c$.

To regularise the cohesive interface, Eq. (1), the infinitesimal surface area $\mathrm{d}A$, at every point $\boldsymbol{x}_c$ on the interface $\Gamma_c$,is rewritten in an integral form

$$\mathrm{d}A\left(\boldsymbol{x}_c\right)=\underbrace{\int_{x_n=-\infty}^{\infty}\delta\left(x_n\right)\mathrm{d}x_n}_{=1}\mathrm{d}A=\int_{x_n=-\infty}^{\infty}\delta\left(x_n\right)\mathrm{d}V\approx\int_{x_n=-\infty}^{\infty}\delta_c\left(x_n\right)\mathrm{d}V \tag{8}$$

where $x_n=\left(\boldsymbol{x}-\boldsymbol{x}_c\right)\cdot\boldsymbol{n}\left(\boldsymbol{x}_c\right)$ and $\boldsymbol{n}\left(\boldsymbol{x}_c\right)$ the unit vector normal to the interface $\Gamma_c$. $\delta\left(x_n\right)$ denotes the Dirac-delta function. The value of $\delta\left(x_n\right)$ is zero everywhere except at $x_n$. In the implementation, it is not possible to regularise the interface by directly employing $\delta\left(x_n\right)$ and we have to use an approximated form of the Dirac-delta function, $\delta_c\left(x_n\right)$, i.e. the last term in Eq. (8). Forms of $\delta_c\left(x_n\right)$ will be discussed in detail in Section 3. Substituting Eq. (8) into (1) yields a regularised energy functional for a cohesive interface:

$$\begin{aligned}\Psi_{\mathrm{pot}}&=\int_{\Omega}\psi^e\left(\boldsymbol{\varepsilon}\left(\mathbf{u}\right)\right)\mathrm{d}V+\int_{\Gamma}\mathcal{G}\left([\![\mathbf{u}]\!],\boldsymbol{\kappa}\right)\int_{x_n=-\infty}^{\infty}\delta\left(x_n\right)\mathrm{d}V\\&=\int_{\Omega}\mathcal{G}\left([\![\mathbf{u}]\!],\boldsymbol{\kappa}\right)\delta\left(x_n\right)\mathrm{d}V\end{aligned} \tag{9}$$

## 3. Phase field representation of cohesive interface

A fundamental issue in the smeared approximation, $\delta_c\left(x_n\right)$ in Eq. (8), is that it is not straightforward to generalise it to more dimensions. Thus we will employ the phase field model to obtain $\delta_c\left(x_n\right)$. The basic idea of the phase field model in the regularised framework is to approximate the discrete interface $\Gamma_c$ by a smeared interface $\Gamma_\xi$, as shown in Fig. 1(b). $\Gamma_\xi$ is associated with a fixed phase field $d\left(\mathbf{x}\right)$ around the interface $\Gamma_c$. $d\left(\mathbf{x}\right)$ equals 1 at the centre of the interface $\Gamma_c$, this is, for $x_n=0$, and vanishes for the domain away from $\Gamma_c$. The phase field distribution is determined by solving the variational problem:

$$d\left(\mathbf{x}\right)=\mathrm{Arg}\left\{\inf_{d\in S_d}\quad\Gamma_\ell\left(d\right)\right\} \tag{10}$$

in which $S_d=\left\{d\,\middle|\,d\left(\mathbf{x}\right)=1\ \forall\mathbf{x}\in\Gamma_c\right\}$ and

$$\Gamma_\ell\left(d\right)=\int_{\Omega}\gamma_d\left(d\right)\mathrm{d}V \tag{11}$$

where $\Gamma_\ell\left(d\right)$ denotes the interface length, i.e. the length of interface per unit area. $\gamma_d\left(d\right)$ represents the crack density function per unit volume.

In the framework of phase field method, following crack density functions are commonly employed:

$$\gamma_d\left(d\right)=\frac{3}{8\ell}d\left(\mathbf{x}\right)+\frac{3\ell}{8}\nabla d\left(\mathbf{x}\right)\cdot\nabla d\left(\mathbf{x}\right)\qquad\text{denoted as AT1 [30]} \tag{12a}$$

$$\gamma_d\left(d\right)=\frac{1}{2\ell}d\left(\mathbf{x}\right)^2+\frac{\ell}{2}\nabla d\left(\mathbf{x}\right)\cdot\nabla d\left(\mathbf{x}\right)\qquad\text{denoted as AT2 [30]} \tag{12b}$$

$$\gamma_d\left(d\right)=\frac{1}{\pi\ell}\left(2d\left(\mathbf{x}\right)-d\left(\mathbf{x}\right)^2\right)+\frac{\ell}{\pi}\nabla d\left(\mathbf{x}\right)\cdot\nabla d\left(\mathbf{x}\right)\qquad\text{denoted as PCM [17]} \tag{12c}$$

in which $\ell$ is a regularisation parameter describing the width of the smeared interface. The Euler–Lagrange equations associated with the variational Eq. (10) read:

$$\text{AT1 [30]}:\begin{cases}1-2\ell^2\dfrac{\mathrm{d}^2d\left(x_n\right)}{\mathrm{d}x_n^2}=0 & x_n\in\mathbb{R}\setminus 0\\ d=1 & x_n=0\\ d=0 & x_n=(-\infty,-2\ell]\bigcup[2\ell,+\infty)\end{cases} \tag{13a}$$

$$\text{AT2 [30]}:\begin{cases}d\left(x_n\right)-\ell^2\dfrac{\mathrm{d}^2d\left(x_n\right)}{\mathrm{d}x_n^2}=0 & x_n\in\mathbb{R}\setminus 0\\ d=1 & x_n=0\\ d=0 & x_n=\pm\infty\end{cases} \tag{13b}$$

$$\text{PCM [17]}:\begin{cases}1-d\left(x_n\right)-\ell^2\dfrac{\mathrm{d}^2d\left(x_n\right)}{\mathrm{d}x_n^2}=0 & x_n\in\mathbb{R}\\ d=1 & x_n=0\\ d=0 & x_n=(-\infty,-\pi\ell/2]\\ & \quad\bigcup[\pi\ell/2,+\infty)\end{cases} \tag{13c}$$

with $x_n=\left(\boldsymbol{x}-\boldsymbol{x}_c\right)\cdot\boldsymbol{n}\left(\boldsymbol{x}_c\right)$, $\boldsymbol{x}_c$ being a point on the interface $\Gamma_c$, $\boldsymbol{n}\left(\boldsymbol{x}_c\right)$ the unit vector normal to the interface $\Gamma_c$. The solutions of Euler–Lagrange equations are, respectively:

$$\text{AT1 [30]}:\quad d\left(x_n\right)=\begin{cases}\left(1-\dfrac{|x_n|}{2\ell}\right)^2 & -2\ell\le x_n\le 2\ell\\ 0 & \text{otherwise}\end{cases} \tag{14a}$$

$$\text{AT2 [30]}:\quad d\left(x_n\right)=\exp\left(-\frac{|x_n|}{\ell}\right) \tag{14b}$$

$$\text{PCM [17]}:\quad d\left(x_n\right)=\begin{cases}1-\sin\left(\dfrac{|x_n|}{\ell}\right) & -\pi\ell/2\le x_n\le\pi\ell/2\\ 0 & \text{otherwise}\end{cases} \tag{14c}$$

Apart from the strong format of the phase field $d\left(x_n\right)$ in Eq. (14) the boundary value problem in Eq. (13) can be solved weakly [11]. Here we take the weak form of Eq. (13c) to illustrate the concept:

$$\begin{aligned}&\int_{-\infty}^{+\infty}\zeta\left(1-d\left(x_n\right)-\ell^2\frac{\mathrm{d}^2d\left(x_n\right)}{\mathrm{d}x_n^2}\right)\mathrm{d}x_n\\&+C\frac{4\ell^2}{h}\int_{-\infty}^{+\infty}\zeta\left(d-1\right)\delta_0\left(x_n\right)\mathrm{d}x_n=0\end{aligned} \tag{15}$$

where $\zeta$ denotes the test function; $C$ is a positive constant, weakly imposing the boundary condition $d=1$ in Eq. (13c); $h$ represents a parameter proportional to the mesh size; $\delta_0\left(x_n\right)$ is the Dirac-delta function used to impose the Dirichlet boundary $d=1$, different from the Dirac-delta function in Eq. (8).

We can now obtain a modified strong form of Eq. (13c), involving the boundary condition $d=1$:

$$\left(\mathcal{F}-1\right)d-\ell^2\frac{\mathrm{d}^2d}{\mathrm{d}x_n^2}=\mathcal{F}-1 \tag{16}$$

with

$$\mathcal{F}=C\frac{4\ell^2}{h}\delta_0\left(x_n\right)\qquad\delta_0\left(x_n\right)=\begin{cases}\dfrac{1}{h}\left(1-\dfrac{|x_n|}{h}\right) & -h\le x_n\le h\\ 0 & \text{otherwise}\end{cases} \tag{17}$$

and the Dirichlet boundary condition reads:

$$d=0\qquad x_n=(-\infty,-\pi\ell/2]\bigcup[\pi\ell/2,+\infty) \tag{18}$$

Eq. (16) has been derived for a one-dimensional setting. It can be extended more dimensions in a straightforward manner. The phase field $d$ then follows from the solution of the weak form:

$$\int_{\Omega}\left[\zeta\left(\mathcal{F}-1\right)d+\ell^2\frac{\partial\zeta}{\partial x_i}\frac{\partial d}{\partial x_i}\right]\mathrm{d}V=\int_{\Omega}\zeta\left(\mathcal{F}-1\right)\mathrm{d}V \tag{19}$$

When solving Eq. (19), we should include the Dirichlet boundary condition in a multi-dimensional setting, i.e. Eq. (18), otherwise the solution is not reliable, see Fig. 2(a). In the figure, AT1 model yields a quadratic distribution of the phase field, satisfying the governing

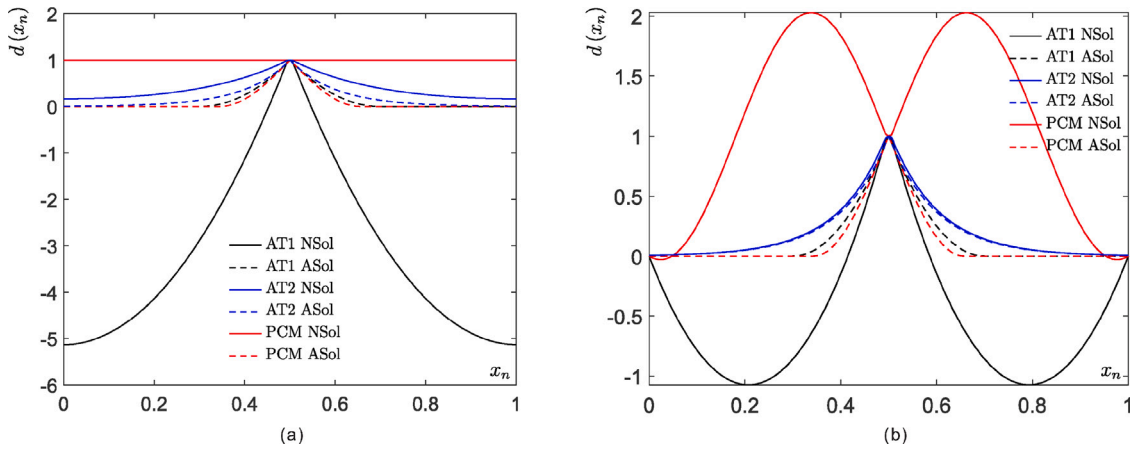


**Fig. 2.** One-dimensional phase field profile $d(x_n)$ for an uniaxial bar (length 1) with an interface $\Gamma_c$ in the centre. The regularisation length is $\ell = 0.1$. The phase field distribution in the case of (a) no consideration of the Dirichlet boundary condition, (b) considering the Dirichlet boundary condition. 'NSol' denotes the results from the weak form, Eq. (19), while 'ASol' represents the analytical results, Eq. (14).

Eq. (13a). However, the phase field value is beyond the range [0, 1]. For the AT2 model, even the phase field value within the range [0, 1], the profile is not consistent with analytical results. In the PCM model, if we do not consider the Dirichlet boundary condition, one possible solution is the homogeneous one, $d = 1$ everywhere in the domain, as presented in Fig. 2(a). However, we should abandon the homogeneous solution in the analysis.

In general, we should consider the Dirichlet boundary condition of Eq. (13) in the domain. However, in the analysis, the boundary condition imposition is not trivial. Fig. 2(b) shows the solution of the phase field $d(x_n)$, with exact boundary condition imposition at two ends of the bar: for the AT1 and PCM model, $d = 0$ at the bar end; for the AT2 model, $d = \exp(-|x_0|/\ell)$ ($|x_0|$ being distance between the interface and the bar end). The numerical solutions for the AT2 model well match the analytical solutions, the maximum difference being 3.26%. For the AT1 and PCM model, the results are different from the analytical solutions. To obtain an acceptable solution, one should set the Dirichlet boundary condition, for instance Eq. (18), exactly in the domain. However, imposing such boundary conditions requires the alignment of the mesh *a priori* with the interface $\Gamma_c$, and element meshes should be set at the Dirichlet boundary interval ends, such as at $x_n = \pm\pi\ell/2$ in Eq. (18). Obviously, such a finite element mesh treatment is not trivial, especially for modelling complicated interface patterns.

Thus, solving Eq. (13) numerically is not a preferred option. Since analytical solutions are available, i.e., Eq. (14), we directly employ them in the analysis. Substituting Eq. (14) into (12) yields the analytical form of the crack density function. We only need to store the distance between the interface and Gauss points once. Then, in the nonlinear solution scheme, we utilise the stored distance and Eq. (12) to compute the crack density function.

In Fig. 3, we have replotted the phase field and the crack density function of the AT1, AT2 and PCM models. For the AT1 and PCM models, the distribution of the phase field and the crack density function is concentrated around the interface $\Gamma_c$, while that of the AT2 model is distributed over the entire domain. In this contribution, we aim to confine the influence of cohesive interface, and we will adopt the phase field function in the PCM model. In line with Eq. (11) the approximated Dirac-delta function in Eq. (8) is formulated as [11]:

$$\delta_c = \frac{1}{\pi\ell}\left(2d(\mathbf{x}) - d(\mathbf{x})^2\right) + \frac{\ell}{\pi}\nabla d(\mathbf{x}) \cdot \nabla d(\mathbf{x}) \tag{20}$$

Obviously, if we substitute this equation in Eq. (8), the smeared interface $\Gamma_\xi$ leads to the exact description of the discrete interface topology $\Gamma_c$ when $\ell \to 0$ [6,7].

## 4. Governing equations

In this section, we will present the construction of the smeared displacement jump and derive the elastic strain in the energy functional. The elastic strain has an identical form to that in the regularised extended finite element method. With the smeared displacement jump, the strong form of the equilibrium will be reformulated.

### 4.1. Smeared displacement jump

In the phase field model, the interface $\Gamma_c$ only exists in a smeared sense. The displacement jump $[\![\mathbf{u}]\!](\boldsymbol{x}_c)$ in the fracture energy function $\mathcal{G}([\![\mathbf{u}]\!], \boldsymbol{\kappa})$ is defined for the discrete interface, see Eq. (4). Thus, we need to regularise the smeared version of the displacement jump $[\![\mathbf{u}]\!](\boldsymbol{x}_c)$. Following the concept of the smeared surface area in Eq. (8), we regularise the displacement jump function using the Dirac-delta function:

$$[\![\mathbf{u}]\!](\boldsymbol{x}_c) = \int_{x_n=-\infty}^{\infty} \boldsymbol{v}(\boldsymbol{x})\,\delta(x_n)\,\mathrm{d}x_n \approx \int_{x_n=-\infty}^{\infty} \boldsymbol{v}(\boldsymbol{x})\,\delta_c(x_n)\,\mathrm{d}x_n \tag{21}$$

with $x_n = (\boldsymbol{x} - \boldsymbol{x}_c)\cdot\boldsymbol{n}(\boldsymbol{x}_c)$, $\boldsymbol{n}(\boldsymbol{x}_c)$ being the unit vector normal to the interface $\Gamma_c$, and $\boldsymbol{v}(\boldsymbol{x})$ an auxiliary field employed to approximate the displacement jump in a smeared sense. Eq. (21) requires that $\boldsymbol{v}(\boldsymbol{x})$ be constant in the direction normal to the interface:

$$\frac{\partial \boldsymbol{v}}{\partial x_n} = 0 \tag{22}$$

which yields

$$\boldsymbol{v}(\boldsymbol{x}) = \boldsymbol{v}(\boldsymbol{x}_c + x_n\boldsymbol{n}) = \boldsymbol{v}(\boldsymbol{x}_c) \tag{23}$$

Considering Eq. (23), the displacement jump $[\![\mathbf{u}]\!](\boldsymbol{x}_c)$ in Eq. (21) is approximated as: $[\![\mathbf{u}]\!](\boldsymbol{x}_c) \approx \boldsymbol{v}(\boldsymbol{x}_c)$. This indicates that the auxiliary field $\boldsymbol{v}$ represents the displacement jump $[\![\mathbf{u}]\!](\boldsymbol{x}_c)$ of the discrete interface. With the PCM model we can introduce the smeared interface in a localised area, $\Gamma_\xi = \{\boldsymbol{x} \in \Omega \mid d(\boldsymbol{x}) > 0\}$, see Fig. 1(b). In the limiting case, i.e., when $\ell \to 0$, the smeared interface $\Gamma_\xi$ is consistent with the discrete interface $\Gamma_c$, and the auxiliary field $\boldsymbol{v}$ coincides with the discrete displacement jump $[\![\mathbf{u}]\!](\boldsymbol{x}_c)$ [11]. In the regularised framework, with the auxiliary field $\boldsymbol{v}$, we can reformulate the energy functional, Eq. (1) as

$$\Psi_{\text{pot}}(\mathbf{u}, \boldsymbol{v}) = \int_\Omega \left(\psi^e(\boldsymbol{\varepsilon}^e) + \mathcal{G}(\boldsymbol{v}, \boldsymbol{\kappa})\,\delta_c + \frac{1}{2}\alpha\left|\frac{\partial \boldsymbol{v}}{\partial x_n}\right|^2\right)\mathrm{d}V \tag{24}$$

with the last term enforcing the constant displacement jump condition in Eq. (22). $\alpha$ is the penalty parameter. Compared to Eq. (1) we have replaced the infinitesimal strain $\boldsymbol{\varepsilon}$ by the 'elastic' strain $\boldsymbol{\varepsilon}^e$. This is due to

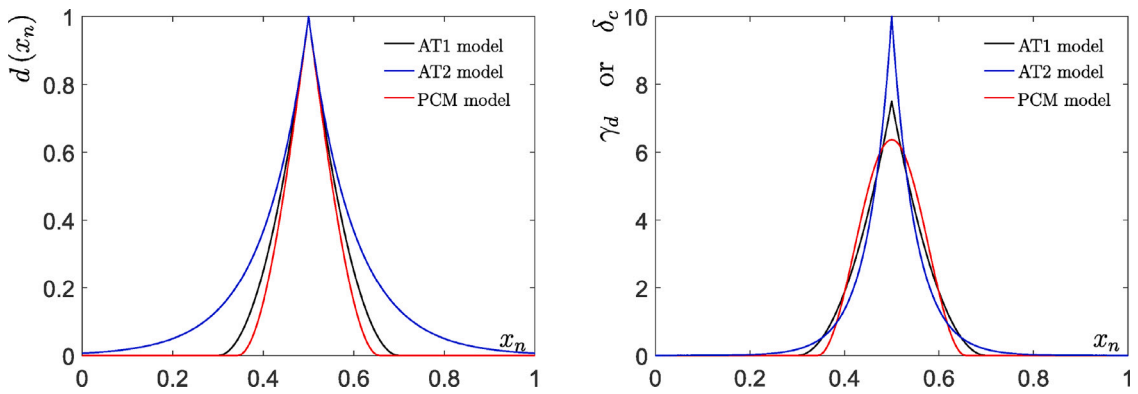


**Fig. 3.** One-dimensional analytical phase field $d(\mathbf{x})$ and crack density $\gamma_c$ profile for an uniaxial bar of unit length 1 with an interface $\Gamma_c$ in the centre. The regularisation length is $\ell = 0.1$.

the smeared representation of the discrete interface $\Gamma_c$, where the clear boundary between the bulk and the interface vanishes. Therefore, the clear distinction between the bulk and interface kinematics, i.e., the infinitesimal strain, Eq. (3), is lost in the velocity of the interface $\Gamma_c$.

### 4.2. Elastic strain and relation to the regularised extended finite element method

Employing the variational principle for minimising $\Psi_{\text{pot}}$ with respect to the displacement $\mathbf{u}$ and the auxiliary field $\boldsymbol{\upsilon}$ results in the weak form of the cohesive interface problem:

$$\delta\Psi_{\text{pot}} = \int_{\Omega} \left( \sigma_{ij}\delta\varepsilon^{e}_{ij} + t_i(\boldsymbol{\upsilon}, \boldsymbol{\kappa})\,\delta_c\delta\upsilon_i + \alpha\frac{\partial\upsilon_i}{\partial x_n}\frac{\partial\delta\upsilon_i}{\partial x_n} \right) \mathrm{d}V = \delta\Psi_{\text{ext}} \tag{25}$$

with the variational form of the energy exerted by the external force:

$$\delta\Psi_{\text{ext}} = \int_{\Gamma_t} \hat{t}_i\delta u_i \mathrm{d}A \tag{26}$$

with $\hat{t}_i$ being the traction along the Neumann boundary $\Gamma_t$. In Eq. (25), the Cauchy stress and cohesive traction are defined as

$$\sigma_{ij} = \frac{\partial\psi^e}{\partial\varepsilon^e_{ij}} \qquad t_i = \frac{\partial\mathcal{G}}{\partial\upsilon_i} \tag{27}$$

Applying the divergence theorem to Eq. (25) yields the elastic strain $\boldsymbol{\varepsilon}^e$ [11]:

$$\varepsilon^e_{ij} = u_{(i,j)} - \text{sym}\left(\upsilon_i n_j\right)\delta_c \tag{28}$$

with $n_j$ being the component of the unit vector normal to the interface $\Gamma_c$. Obviously, the 'elastic' strain $\boldsymbol{\varepsilon}^e$ is composed of the gradient of the displacement and the term related to the displacement jump.

In deriving Eq. (28) we employed a variational principle. We can also arrive at Eq. (28) using the extended finite element method (XFEM). Recalling the displacement function in the XFEM we have a continuous part, $\mathbf{v}(\boldsymbol{x})$, and a bounded part that modulates the displacement jump over the domain through the Heaviside function $\mathscr{H}$ [31]:

$$\mathbf{u}(\boldsymbol{x}) = \mathbf{v}(\boldsymbol{x}) + \mathscr{H}(\boldsymbol{x})\,\mathbf{a}(\boldsymbol{x}) \tag{29}$$

with $\mathbf{a}(\boldsymbol{x})$ being the displacement jump. Considering the small strain assumption, the infinitesimal strain field becomes [32]:

$$\varepsilon_{ij} = u_{(i,j)} = \mathrm{v}_{(i,j)} + \mathscr{H}\mathrm{a}_{(i,j)} + \text{sym}\left(\mathrm{a}_i n_j\right)\delta_\Gamma \tag{30}$$

with $\delta_\Gamma$ being the Dirac-delta function. Eq. (30) is thus expressed as the sum of a bounded bulk term $\boldsymbol{\varepsilon}^b$ and a localised term $\boldsymbol{\varepsilon}^\rho$:

$$\varepsilon_{ij} = u_{(i,j)} = \varepsilon^b_{ij} + \varepsilon^\rho_{ij} \quad \text{with} \quad \varepsilon^b_{ij} = \mathrm{v}_{(i,j)} + \mathscr{H}\mathrm{a}_{(i,j)} \qquad \varepsilon^\rho_{ij} = \text{sym}\left(\mathrm{a}_i n_j\right)\delta_\Gamma \tag{31}$$

When we regularise the cohesive interface starting from the extended finite element framework, we also arrive at the 'elastic' strain in Eq. (28) by taking the form:

$$\varepsilon^b_{ij} = u_{(i,j)} - \varepsilon^\rho_{ij} \quad \Rightarrow \quad \varepsilon^e_{ij} = \varepsilon^b_{ij} \qquad \text{and} \qquad \text{sym}\left(\upsilon_i n_j\right)\delta_c = \varepsilon^\rho_{ij} \tag{32}$$

Obviously, the elastic strain derived in Eq. (28) is equal to that in the regularised extended finite element method.

### 4.3. Strong form of the boundary value problem

Substituting Eq. (28) into Eq. (25) leads to

$$\int_{\Omega} \left( \sigma_{ij}\delta\mathrm{u}_{(i,j)} - \delta_c\sigma_{ij}\text{sym}\left(\delta\upsilon_i n_j\right) + t_i(\boldsymbol{\upsilon}, \boldsymbol{\kappa})\,\delta_c\delta\upsilon_i + \alpha\frac{\partial\upsilon_i}{\partial x_n}\frac{\partial\delta\upsilon_i}{\partial x_n} \right) \mathrm{d}V = \int_{\Gamma_t} \hat{t}_i\delta u_i \mathrm{d}A \tag{33}$$

Applying integration by parts we can reformulate Eq. (33) as:

$$\int_{\Omega} \left( -\frac{\sigma_{ij}}{\partial x_j}\delta u_i - \left[ \delta_c\left(\sigma_{ij}n_j - t_i(\boldsymbol{\upsilon}, \boldsymbol{\kappa})\right) + \alpha\frac{\partial^2\upsilon_i}{\partial x_n^2} \right]\delta\upsilon_i \right) \mathrm{d}V = \int_{\Gamma_t} \left(\hat{t}_i - \sigma_{ij}n_j\right)\delta u_i \mathrm{d}A - \int_{\partial\Gamma_\xi} \alpha\frac{\partial\upsilon_i}{\partial x_n}\delta\upsilon_i \mathrm{d}A \tag{34}$$

where $\partial\Gamma_\xi$ denotes the smeared interface boundary. Considering a variation in the displacement field and the displacement jump field, respectively, subsequently yields the strong form of the cohesive interface problem in the framework of the phase field method:

$$\begin{cases} \dfrac{\partial\sigma_{ij}}{\partial x_j} = 0 & \boldsymbol{x} \in \Omega \\ \sigma_{ij}n_j = \hat{t}_i & \boldsymbol{x} \in \Gamma_t \end{cases} \tag{35a}$$

$$\begin{cases} \delta_c\left(t_i(\boldsymbol{\upsilon}, \boldsymbol{\kappa}) - \sigma_{ij}n_j\right) = \alpha\dfrac{\partial^2\upsilon_i}{\partial x_n^2} & \boldsymbol{x} \in \Gamma_\xi \\ \dfrac{\partial\upsilon_i}{\partial x_n} = 0 & \boldsymbol{x} \in \partial\Gamma_\xi \end{cases} \tag{35b}$$

Eq. (35a) is standard in the continuum mechanics, supplemented with the constitutive relation, Eq. (27). Eq. (35b) is a supplementary equation for the smeared interface problem. It represents equilibrium over the smeared interface. In the limiting case, i.e., when $\ell \to 0$, the discrete cohesive traction is recovered from Eq. (35b): $t_i(\llbracket\mathbf{u}\rrbracket, \boldsymbol{\kappa}) = \sigma_{ij}n_j$. The penalty term enforces the constant displacement jump in the direction perpendicular to the interface $\Gamma_c$. The boundary condition in Eq. (35b) requires that the displacement jump at the boundary of the smeared interface, $\partial\Gamma_\xi$, should also be constant. This condition necessitates fully prescribed displacement jump degrees of freedom in the entire domain $\Omega$. We will illustrate this by a numerical study in Section 5.

## 5. Finite element implementation

For the spatial discretisation we exploit $C^1$-continuous Powell–Sabin B-splines [33,34]. A flexible control of the geometry is possible, such as remeshing using any standard package for triangular elements [35], while the $C^1$-continuity assures an improved stress prediction [36]. Powell–Sabin B-splines describe the geometry and interpolate the displacement field $\mathbf{u}$ and the displacement jump $\boldsymbol{\upsilon}$ in an isoparametric sense [33]:

$$\begin{aligned} \boldsymbol{x} &= \sum_{k=1}^{N_t}\sum_{j=1}^{3} N_k^j \boldsymbol{X}_k^j = \boldsymbol{N}\boldsymbol{X} \qquad \mathbf{u} = \sum_{k=1}^{N_t}\sum_{j=1}^{3} N_k^j \boldsymbol{U}_k^j = \boldsymbol{N}\boldsymbol{U} \\ \boldsymbol{\upsilon} &= \sum_{i=1}^{N_\upsilon}\sum_{j=1}^{3} N_i^j \boldsymbol{\vartheta}_i^j = \boldsymbol{N}_\upsilon \boldsymbol{\vartheta}, \end{aligned} \tag{36}$$

where $\boldsymbol{X}_k^j$ represent the coordinates of the corners $\boldsymbol{Q}_k^j$ of the Powell–Sabin triangles, $\boldsymbol{U}_k^j$ denote the displacement dofs at $\boldsymbol{Q}_k^j$, and $N_t$ is the total number of vertices in the whole domain. $\boldsymbol{\vartheta}_i^j$ is the displacement jump dofs at the corner $\boldsymbol{Q}_i^j$, and $N_\upsilon$ is the number of vertices in the domain with prescribed displacement jump dofs, e.g., blue area $\Gamma_\xi$ in Fig. 4(b). The indices $j = 1, 2, 3$ imply that three Powell–Sabin B-splines $N_k^j$ are defined on each vertex $k$. $\boldsymbol{N}$ and $\boldsymbol{N}_\upsilon$ are the shape function matrix. $\boldsymbol{X}$, $\boldsymbol{U}$ and $\boldsymbol{\vartheta}$ are the vector of the coordinates, the displacement, and the displacement jump, respectively.

A limitation of Powell–Sabin B-splines lies in the extension to three-dimensional objects. Until now, there is no procedure to define Powell–Sabin B-splines on arbitrary tetrahedral meshes because of certain constraints with neighbouring tetrahedrons [37], and they only work for structured meshes. Alternatively, one can construct prisms as a tensor product of two-dimensional Powell–Sabin B-splines and Non-Uniform Rational Basis splines (NURBS) in the third dimension.

The interpolation function in (36) yields following relations:

$$\mathrm{sym}\left(\frac{\partial \mathbf{u}}{\partial \boldsymbol{x}}\right) = \boldsymbol{B}_u \boldsymbol{U} \qquad \mathrm{sym}\left(\boldsymbol{\upsilon}\otimes\boldsymbol{n}\right) = \boldsymbol{B}_\upsilon \boldsymbol{\vartheta} \qquad \frac{\partial \boldsymbol{\upsilon}}{\partial x_n} = \boldsymbol{G}_\upsilon \boldsymbol{\vartheta} \tag{37}$$

with all tensorial quantities are written in Voigt notation.

With this discretisation the following system of non-linear equations is obtained:

$$\begin{cases} \boldsymbol{F}_{\mathrm{int},u}\left(\boldsymbol{U},\boldsymbol{\vartheta}\right) = \boldsymbol{F}_{\mathrm{ext},u} \\ \boldsymbol{F}_{\mathrm{int},\upsilon}\left(\boldsymbol{U},\boldsymbol{\vartheta}\right) = \boldsymbol{0} \end{cases} \tag{38}$$

the internal force vectors being:

$$\begin{cases} \boldsymbol{F}_{\mathrm{int},u}\left(\boldsymbol{U},\boldsymbol{\vartheta}\right) = \int_\Omega \boldsymbol{B}_u^{\mathrm{T}}\left(\mathbf{D}\boldsymbol{B}_u\boldsymbol{U} - \delta_c \mathbf{D}\boldsymbol{B}_\upsilon\boldsymbol{\vartheta}\right)\mathrm{d}V \\ \boldsymbol{F}_{\mathrm{int},\upsilon}\left(\boldsymbol{U},\boldsymbol{\vartheta}\right) = \int_\Omega \left[-\delta_c \boldsymbol{B}_\upsilon^{\mathrm{T}}\left(\mathbf{D}\boldsymbol{B}_u\boldsymbol{U} - \delta_c \mathbf{D}\boldsymbol{B}_\upsilon\boldsymbol{\vartheta}\right) + \delta_c \boldsymbol{N}^{\mathrm{T}}\mathbf{t}\left(\boldsymbol{\upsilon},\boldsymbol{\kappa}\right) + \alpha \boldsymbol{G}_\upsilon^{\mathrm{T}}\boldsymbol{G}_\upsilon\boldsymbol{\vartheta}\right]\mathrm{d}V \end{cases} \tag{39}$$

and $\mathbf{D}$ being the elasticity matrix, $\delta_c$ being the approximated Dirac-delta function defined in Eq. (20).

Finally, the system Eq. (38) is solved by a standard Newton–Raphson procedure with the tangent stiffness matrix:

$$\mathbf{K} = \begin{bmatrix} \mathbf{K}_{uu} & \mathbf{K}_{u\upsilon} \\ \mathbf{K}_{\upsilon u} & \mathbf{K}_{\upsilon\upsilon} \end{bmatrix} \tag{40}$$

with

$$\begin{aligned} \mathbf{K}_{uu} &= \frac{\partial \boldsymbol{F}_{\mathrm{int},u}}{\partial \boldsymbol{U}} = \int_\Omega \boldsymbol{B}_u^{\mathrm{T}}\mathbf{D}\boldsymbol{B}_u \mathrm{d}V \\ \mathbf{K}_{u\upsilon} &= \frac{\partial \boldsymbol{F}_{\mathrm{int},u}}{\partial \boldsymbol{\vartheta}} = \int -\delta_c \boldsymbol{B}_u^{\mathrm{T}}\mathbf{D}\boldsymbol{B}_\upsilon \mathrm{d}V \\ \mathbf{K}_{\upsilon u} &= \frac{\partial \boldsymbol{F}_{\mathrm{int},\upsilon}}{\partial \boldsymbol{U}} = \int -\delta_c \boldsymbol{B}_\upsilon^{\mathrm{T}}\mathbf{D}\boldsymbol{B}_u \mathrm{d}V \\ \mathbf{K}_{\upsilon\upsilon} &= \frac{\partial \boldsymbol{F}_{\mathrm{int},\upsilon}}{\partial \boldsymbol{U}} = \int \left(\delta_c^2 \boldsymbol{B}_\upsilon^{\mathrm{T}}\mathbf{D}\boldsymbol{B}_\upsilon + \delta_c \boldsymbol{N}^{\mathrm{T}}\frac{\partial \mathbf{t}\left(\boldsymbol{\upsilon},\boldsymbol{\kappa}\right)}{\partial \boldsymbol{\upsilon}} + \alpha \boldsymbol{G}_\upsilon^{\mathrm{T}}\boldsymbol{G}_\upsilon\right)\mathrm{d}V \end{aligned} \tag{41}$$

In the numerical implementation, we should consider how to prescribe the displacement jump degrees of freedom in the domain. Obviously, we could either fully assign them in the entire domain, similar to the displacement degrees of freedom, or partially assign them in a narrow area around the interface, see Fig. 4(b). Now, we will carry out a numerical test to assess both methods. Here, a two-dimensional version of a uniaxial tension problem is revisited, see Fig. 4(a), to study the solutions of a 1D bar with an interface [11]. Fig. 4(a) shows the geometry and boundary conditions. With a suitable rescaling of the loading, we can set Young's modulus $E_0 = 1.0$, Poisson's ratio $\nu = 0.0$. A unit cross-sectional area $A = 1$ is considered with a height $H = 1$ and a length $L = 1$. The interface $\Gamma_c$ is prescribed in the middle of the plate. The fracture energy is given as $\mathcal{G}\left(\upsilon_1, \kappa\right) = \frac{1}{2}k\upsilon_1^2$, yielding the traction $t_1 = k\upsilon_1$. The interface stiffness $k$ is set as $k = 1$. The penalty parameter in Eq. (24) is assigned $\alpha = 1$. The regularisation length is chosen as $\ell = 0.1$. The analytical solutions of the displacement, the displacement jump and the stress read:

$$\begin{aligned} u_1\left(x_1, x_2\right) &= \begin{cases} \dfrac{\bar{u}_1 k x_1}{kL+E} & 0 \le x_1 \le L_1^- \\ \dfrac{\bar{u}_1 k x_1}{kL+E} + \dfrac{\bar{u}_1 E}{kL+E} & L_1^+ \le x_1 \le L \end{cases} \\ [\![u]\!] = \upsilon_1 &= \frac{\bar{u}_1 E}{kL+E} \qquad \sigma_1\left(x_1, x_2\right) = \frac{\bar{u}_1 kE}{kL+E} \end{aligned} \tag{42}$$

where $L_1^-$ and $L_1^+$ are the left and right side of the interface $\Gamma_c$.

Fig. 5 shows the comparison between numerical and analytical solutions. The results for the fully assigned displacement jump degrees of freedom agree well with analytical solutions. For the displacement, the numerical solution for fully assigned degrees of freedom has a small discrepancy in the range of the smeared interface $\Gamma_\xi$, which is due to the regularised interface and continuous field variables in the phase field method.

For partially assigned displacement jump degrees of freedom, Fig. 4(b), the results deviate from the analytical solutions, see Fig. 5. The displacement jump $\upsilon_1\left(x_1, 0\right)$ is not constant, Fig. 5(a), violating the constant displacement jump assumption in Eq. (22). If we partially prescribe displacement jump degrees of freedom in the smeared interface $\Gamma_\xi$, then $\upsilon_1\left(x_1, 0\right)$ will be zero outside $\Gamma_\xi$. In the present numerical framework, field variables, here displacement and displacement jump, should be continuous in the entire domain, see Eq. (36). Then, $\upsilon_1\left(x_1, 0\right)$ will attain a maximum in the centre of the smeared interface $\Gamma_\xi$ and be zero at the boundary $\partial\Gamma_\xi$, as illustrated in Fig. 5(a). In this figure the displacement is almost constant outside $\Gamma_\xi$. This is due to the zero displacement jump outside $\Gamma_\xi$. From Eq. (35b) we have the traction balance relation $t_i\left(\boldsymbol{\upsilon},\boldsymbol{\kappa}\right) = \sigma_{ij}n_j$. If the displacement jump $\boldsymbol{\upsilon} = 0$, then the traction $t_i\left(\boldsymbol{\upsilon},\boldsymbol{\kappa}\right)$ should be zero in this numerical test. Consequently, the stress $\sigma_1\left(x_1, 0\right)$ should be zero, as demonstrated in Fig. 5(b). If there is no stress outside $\Gamma_\xi$, then the displacement will be constant due to the rigid body motion, as shown in Fig. 5(a).

In sum, we should fully prescribe the displacement jump degrees of freedom in the entire domain. Then, the displacement jump approximation equation in Eq. (36) should be modified as

$$\boldsymbol{\upsilon} = \sum_{k=1}^{N_t}\sum_{j=1}^{3} N_k^j \boldsymbol{\vartheta}_k^j = \boldsymbol{N}\boldsymbol{\vartheta} \tag{43}$$

where $N_t$, $N_k^j$ and $\boldsymbol{N}$ are defined in Eq. (36).

In cases where an area is not 'visible' from the interface $\Gamma_c$, e.g., the green areas $\Omega_n$ in Fig. 6(b), we still must prescribe the displacement jump degrees of freedom in $\Omega_n$. When evaluating the stiffness matrix in Eq. (41) we need to compute the normal vector $\boldsymbol{n}$ with respect to the interface. For the area $\Omega_n$, invisible to the interface $\Gamma_c$, we only need to take the normal vector, $\boldsymbol{n}^C$ of point $C$ in Fig. 6(b), with respect to extended tangent lines of a closest interface (shortest distance to the interface), see the dotted lines $\Gamma_c^e$ in Fig. 6(b). We could also get the normal distance of point $C$ from the relation: $x_n^C = \left(\boldsymbol{x}^C - \boldsymbol{x}^D\right)\cdot\boldsymbol{n}^C$ (point

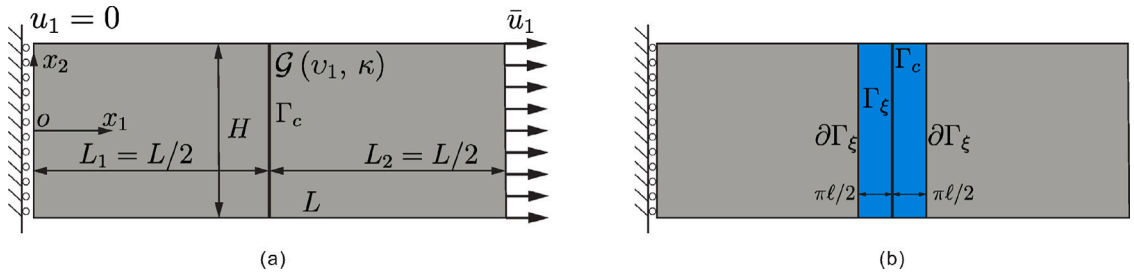


**Fig. 4.** (a) uniaxial traction of a bar with an interface $\Gamma_c$; (b) smeared interface $\Gamma_\xi$ (blue area), which is prescribed with the displacement jump degrees of freedom. For the PCM model, due to the narrow distribution of the phase field, we can locally prescribe the displacement jump degrees of freedom in the domain around the interface, $\Gamma_\xi$.

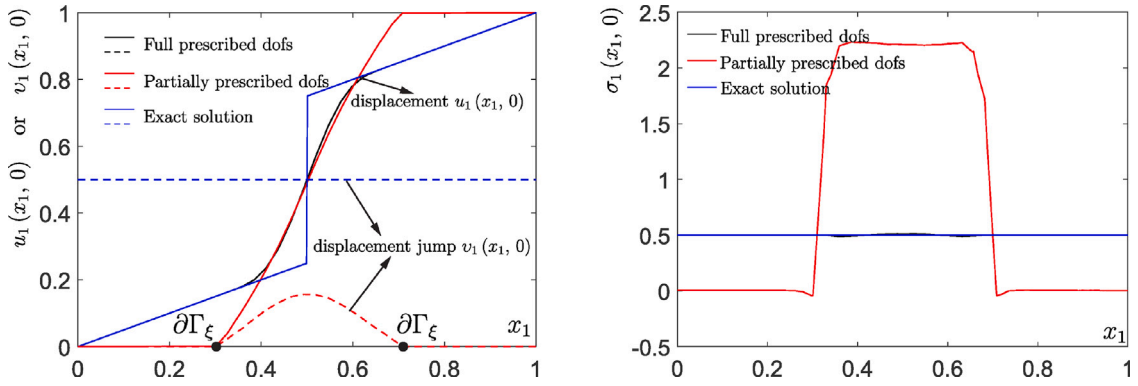


**Fig. 5.** Displacement $u_1$, displacement jump $\upsilon_1$ and stress $\sigma_1$ for the uniaxial bar in Fig. 4(a). Black dots denote the boundary $\partial\Gamma_\xi$ of the smeared interface $\Gamma_\xi$. Here, we consider the fracture energy function $\mathcal{G}(\upsilon_1, \kappa) = \frac{1}{2}k(\upsilon_1)^2$. The imposed end-displacement is $\bar{u}_1 = 1$. The regularisation length is $\ell = 0.1$.

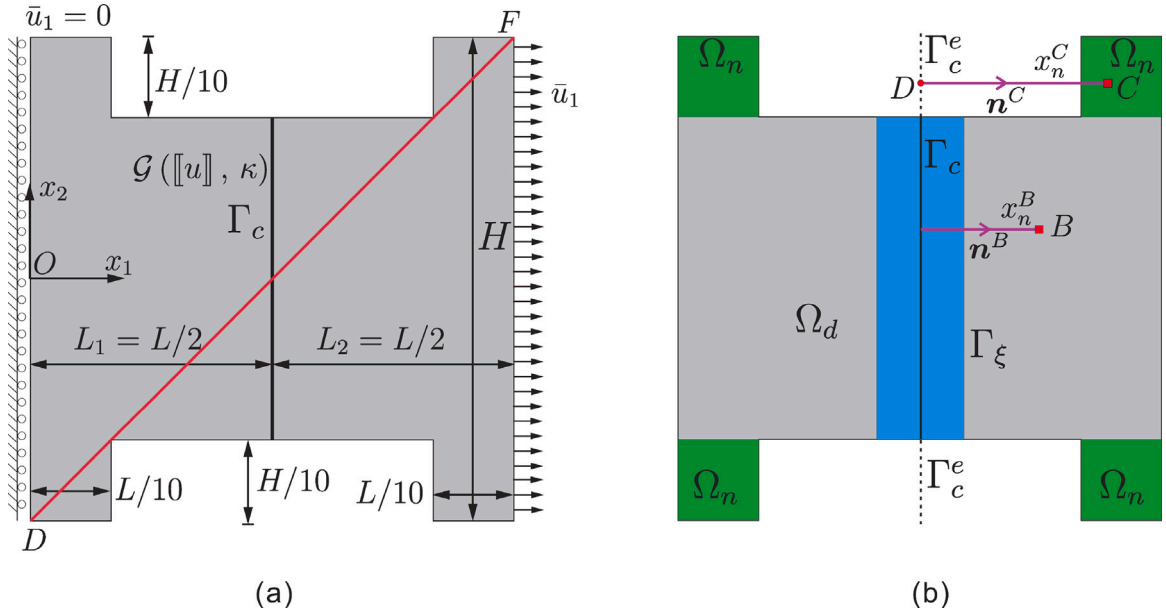


**Fig. 6.** (a) axial traction of a 'H'-shaped plate with an interface $\Gamma_c$; (b) area 'visible' and 'invisible' from the interface $\Gamma_c$. The area $\Omega_n$ is not 'visible' from $\Gamma_c$, while the area $\Omega_d$ is 'visible' from the interface. $x_n$ denotes the distance of a point to the interface. The blue area indicates the smeared interface $\Gamma_\xi$.

$D$ being foot point from point $C$ to the extended interface $\Gamma_c^e$). In the stiffness matrix Eq. (41), for the invisible area $\Omega_n$, the delta function will be $\delta_c = 0$, only the term $\alpha \boldsymbol{G}_\upsilon^{\mathrm{T}} \boldsymbol{G}_\upsilon$ will be remain, complying with the normal vector $\boldsymbol{n}^C$. For the domain visible to the interface, $\Omega_d$ in Fig. 6(b), the evaluation of the normal vector ($\boldsymbol{n}^B$) and the normal distance ($x_n^C$) can be carried out normally.

The imposition of displacement jump degrees of freedom may be tedious for complex interface patterns. However, we only need to save the normal vector and the distance between the interface and Gauss points once in the pre-processing stage. Then, during the solution phase, we use the saved distance and normal vector to compute the stiffness matrix. Hence, the computational efficiency does not suffer much.

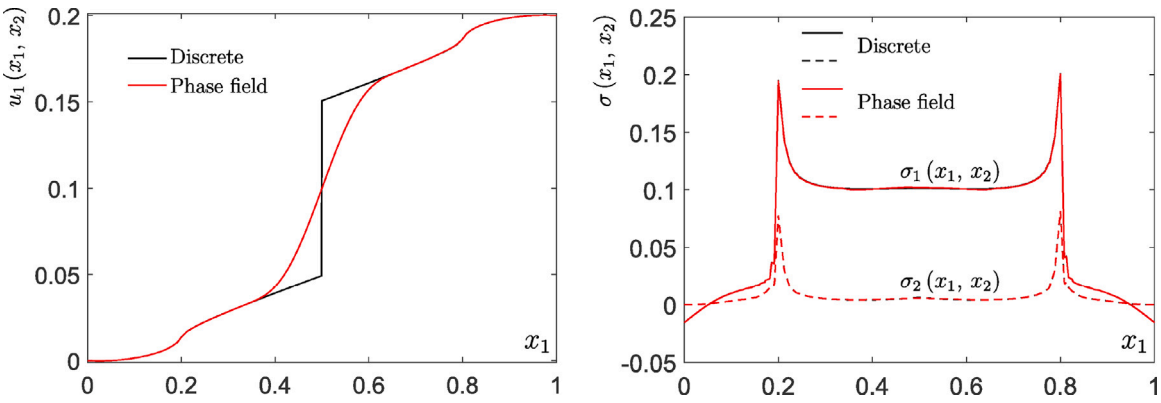


**Fig. 7.** Displacement $u_1$ and stress $\sigma$ along the diagonal line $DF$ in Fig. 6(a).

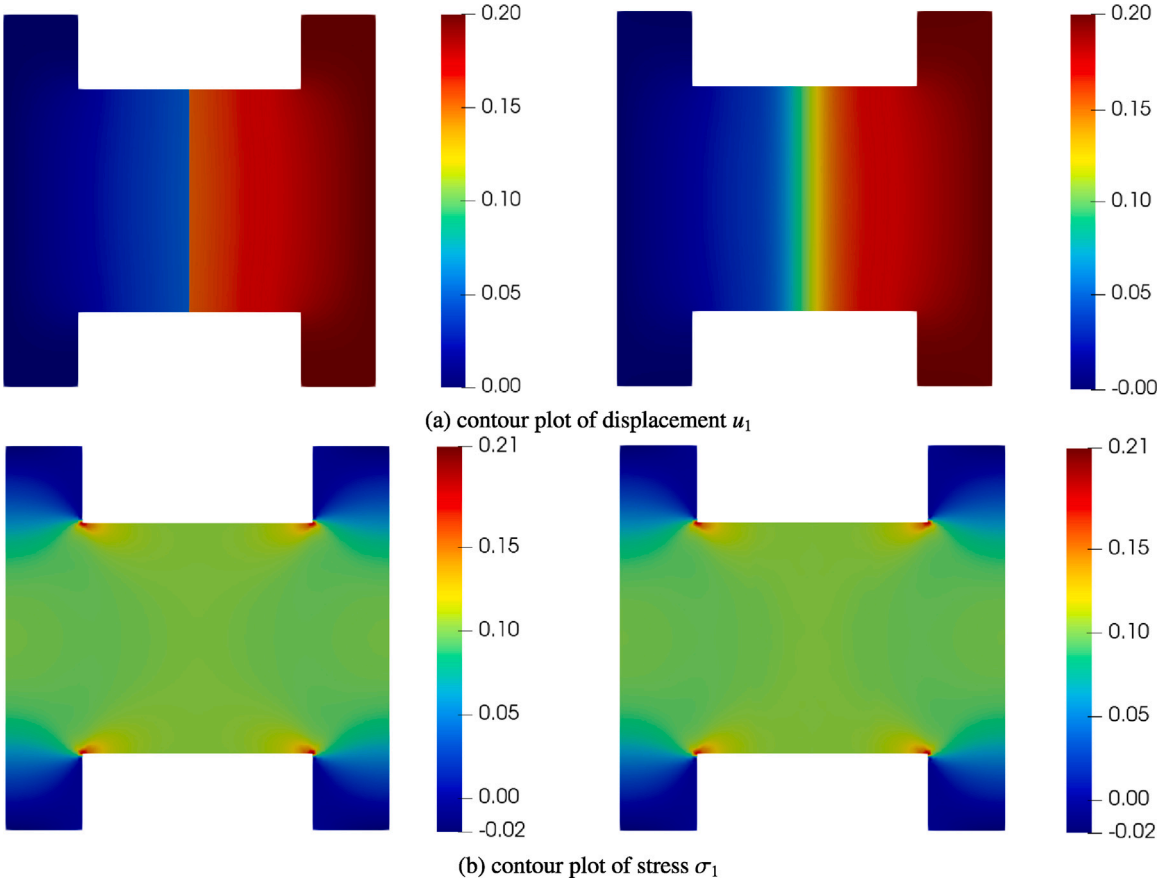


**Fig. 8.** Contour plot of displacement $u_1$ and stress $\sigma_1$. The figures in the left column represent the solution of the discrete interface model, while the figures in the right column represent the solution of the present method.

To validate the proposed concept, we consider the 'H'-shaped plate of Fig. 6(a). We use the same material properties as in the uniaxial traction example in Fig. 4. We consider the solution of the discrete interface model as the reference solution [29]. Fig. 7 shows the comparison between the discrete and proposed model. The displacement $u_1$ and stress $\sigma$ along the diagonal line $DF$ in Fig. 6(a) are shown. Clearly, the displacement and stress computed using the present model match well with those of the discrete interface model, of course except for the displacement within the smeared interface $\Gamma_\xi$. The displacement plot shows a jump at the interface $\Gamma_c$ in the discrete model, while it is smooth along $DF$ in the smeared interface model, due to the regularisation. The contour plots of the displacement $u_1$ and stress $\sigma_1$ are illustrated in Fig. 8. Obviously, the stresses are consistent, while the displacement shows some discrepancy in the range of the smeared interface $\Gamma_\xi$.

For the area $\Omega_n$, even the interface $\Gamma_c$ is not visible, we could still impose the displacement jump dofs here. The solutions are consistent with those from the discrete interface model. The balance Eq. (35b) is still satisfied with the imposed displacement jump dofs. For the visible area $\Omega_d$, we have the traction balance relation $t_i(\boldsymbol{v}, \boldsymbol{\kappa}) = \sigma_{ij} n_j$ and the Dirac-delta function $\delta_c = 0$ outside the smeared interface $\Gamma_\xi$. For the invisible area $\Omega_n$, the traction balance relation $t_i(\boldsymbol{v}, \boldsymbol{\kappa}) = \sigma_{ij} n_j$

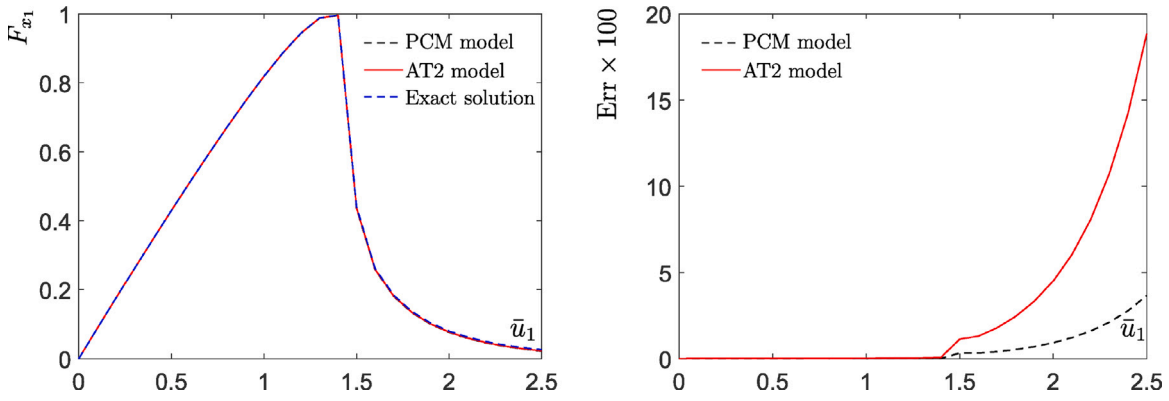


**Fig. 9.** Force–displacement curve and the error. Err is the error of the numerical solution, Err = $\frac{F_{x_1}^{\text{num}} - F_{x_1}^{\text{ext}}}{F_{x_1}^{\text{ext}}}$, where 'num' denotes the numerical results from the PCM and AT2 model, 'ext' represents the exact solution.

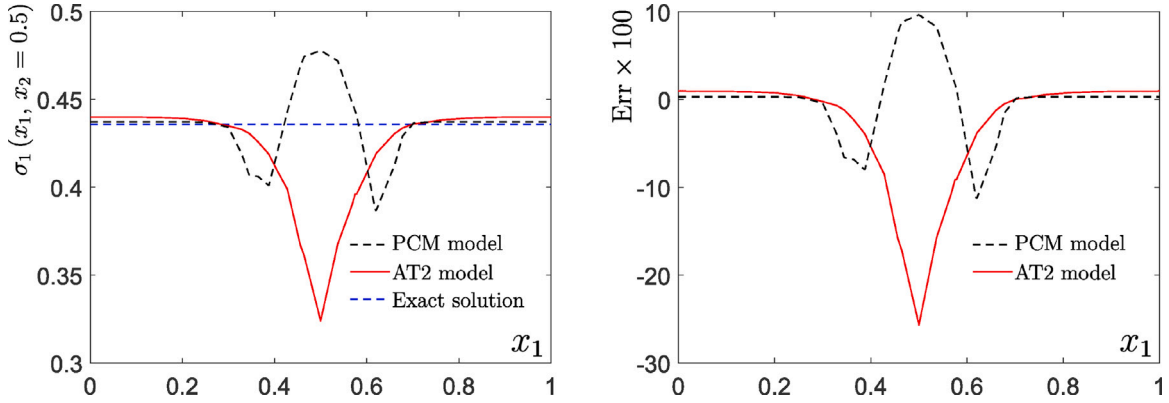


**Fig. 10.** The stress $\sigma_1$ along the centre plane and the error in the case of a prescribed displacement $\bar{u}_1 = 1.5$. Err is the error of the numerical solution, Err = $\frac{\sigma_1^{\text{num}} - \sigma_1^{\text{ext}}}{\sigma_1^{\text{ext}}}$, where 'num' denotes the numerical results from the PCM and AT2 models, 'ext' represents the exact solution.

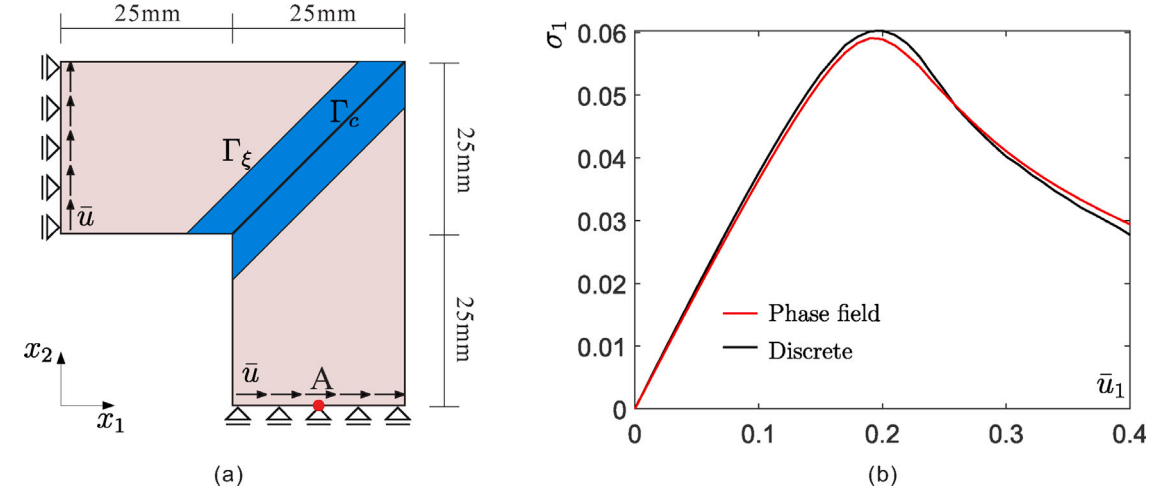


**Fig. 11.** (a) geometry and boundary conditions of L-shaped beam, where the blue area indicates the smeared interface $\Gamma_\xi^*$; (b) response curves for the L-shaped beam. The stress component $\sigma_1$ at $\boldsymbol{x}_A = (37.5,\ 0)$ mm is plotted vs the prescribed displacement $\bar{u}$. A discrete interface model is employed to provide the reference solution.

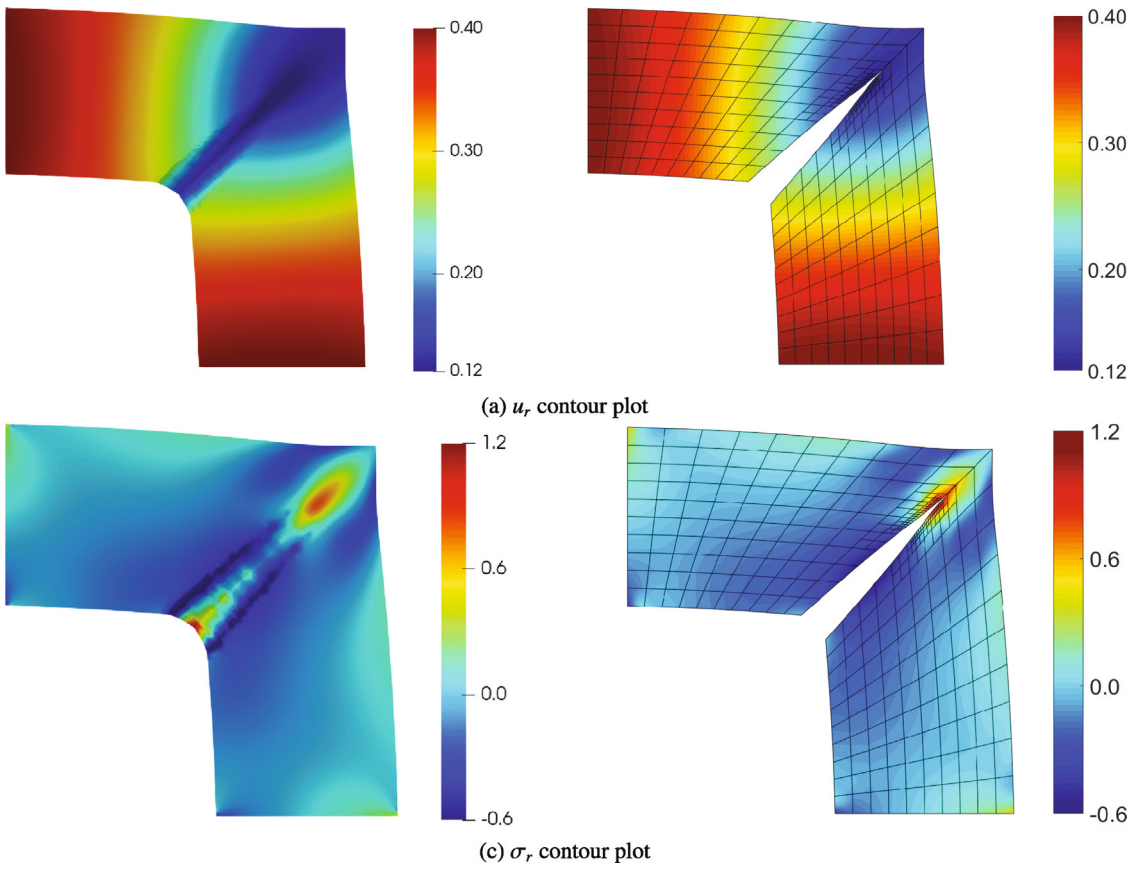


**Fig. 12.** Distribution of the radial displacement $u_r$ and the radial stress $\sigma_r$ in the beam subject to the loading $\bar{u} = 0.4$ *mm*. The displacements have been amplified by a factor 10. The left column denotes the solution of the present method, while the right column represents the solution of the discrete interface model.

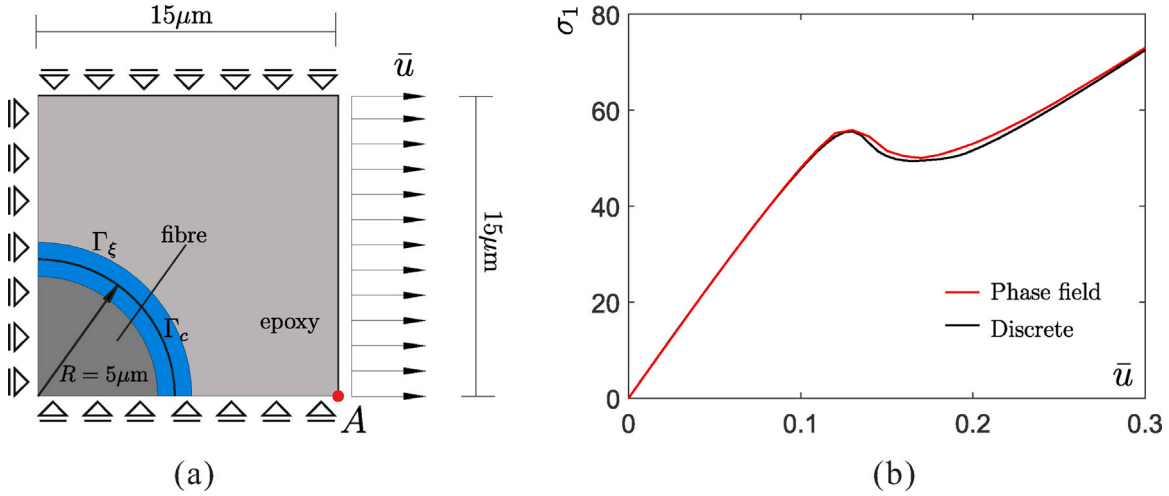


**Fig. 13.** (a) geometry and boundary conditions of one quarter of the fibre [38], where the blue area indicates the smeared interface $\Gamma_\xi$; (b) response curves for the plate. The stress component $\sigma_1$ at $\boldsymbol{x}_A = (15,\ 0)\,\mu$m is plotted *vs* the prescribed displacement $\bar{u}$. A discrete interface model is employed to provide the reference solution.

maybe not satisfied, however the Dirac-delta function $\delta_c$ equals zero, guaranteeing the balance Eq. (35b).

## 6. Numerical examples

To investigate the performance of the approach, three examples are presented. First, we will consider a two-dimensional version of a uniaxial tension example to study the solution of a 1D bar with an interface [11]. Then, a delamination peel test of an L-shaped beam is taken to demonstrate the applicability of the method in two dimensions. Finally, a fibre–epoxy debonding test is considered to explore interface debonding under mixed-mode loading conditions, demonstrating the ability of the method to analyse curved interfaces.

### 6.1. Uniaxial traction of a bar

We again consider the two-dimensional version of a uniaxial tension example in Fig. 4, but now with a cohesive interface. The behaviour of

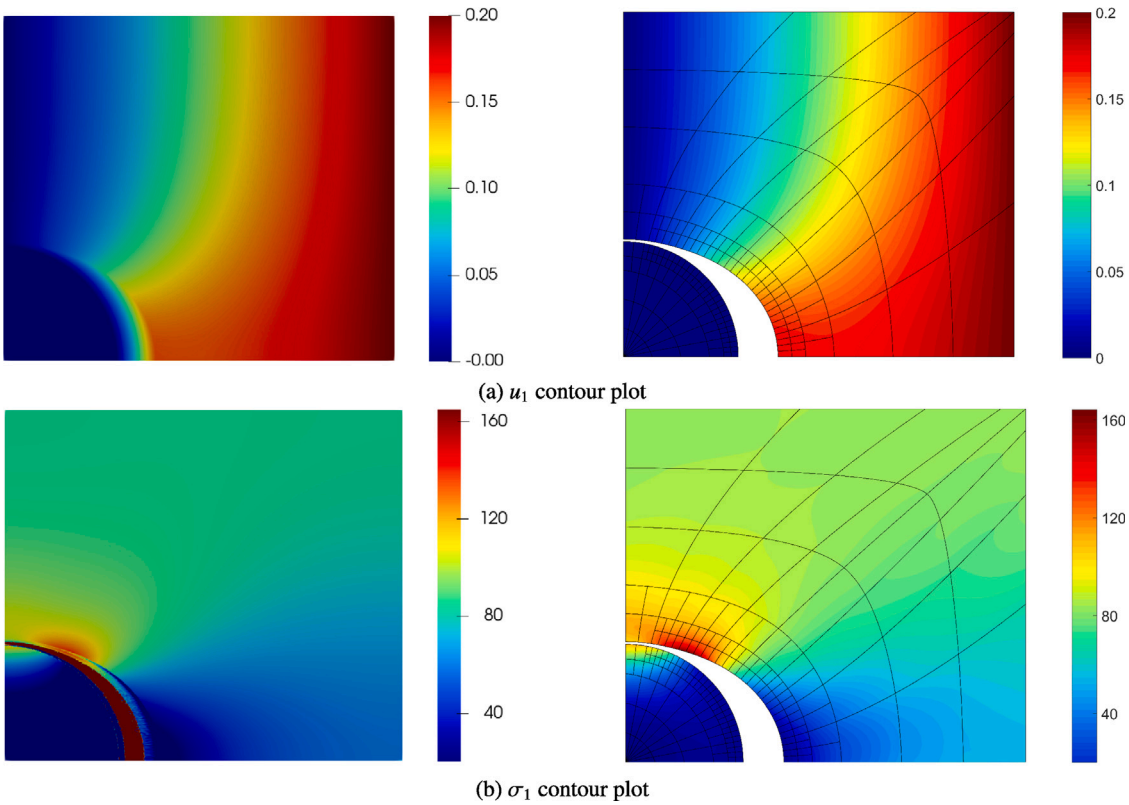


**Fig. 14.** Distribution of the displacement $u_1$ and the stress $\sigma_1$ under the loading $\bar{u} = 0.2$ μm. The displacements have been amplified by a factor 10. The left column denotes the solution of phase field method, while the right column represents the solution of the discrete interface model.

the interface is described by the Xu–Needleman law of Eq. (6). For this problem, only mode-I loadings are included in the analysis. Then, the interface energy and traction are taken as

$$\mathcal{G} = \mathcal{G}_c \left[1 - \left(1 + \frac{\upsilon_1}{\delta_n}\right) \exp\left(-\frac{\upsilon_1}{\delta_n}\right)\right] \qquad t_n = \frac{\mathcal{G}_c}{\delta_n}\frac{\upsilon_1}{\delta_n} \exp\left(-\frac{\upsilon_1}{\delta_n}\right) \quad (44)$$

with $\upsilon_1$ being the displacement jump in the $x_1$-direction.

With a suitable rescaling of the loading, we can set Young's modulus $E_0 = 1.0$, Poisson's ratio $\nu = 0.0$, the fracture toughness $\mathcal{G}_c = 1$ and the fracture strength $t_u = 1$. A unit cross-sectional area $A = 1$ is considered with a height $H = 1$ and a length $L = 1$. The penalty parameter in Eq. (24) is set as $\alpha = t_u$. The regularisation length is given as $\ell = 0.1$. The displacement jump $\upsilon_1$ cannot be solved analytically, as there exists no explicit expression due to the transcendental form of the traction equation. So it is solved numerically on the basis of the analytical equation:

$$\frac{L}{E}\frac{\mathcal{G}_c}{\delta_n}\frac{\upsilon_1}{\delta_n} \exp\left(-\frac{\upsilon_1}{\delta_n}\right) + \upsilon_1 = \bar{u}_1 \quad (45)$$

which yields the solutions of the displacement and the stress:

$$u_1(x_1, x_2) = \begin{cases} \dfrac{t_n x_1}{E} & 0 \le x_1 \le L_1^- \\ \dfrac{t_n x_1}{E} + \upsilon_1 & L_1^+ \le x_1 \le L \end{cases} \quad (46)$$

$$\sigma_1(x_1, x_2) = t_n = \frac{\mathcal{G}_c}{\delta_n}\frac{\upsilon_1}{\delta_n} \exp\left(-\frac{\upsilon_1}{\delta_n}\right)$$

where $L_1^-$ and $L_1^+$ are the left and right side of the interface $\Gamma_c$, respectively.

Figs. 9 and 10 show the comparison between the numerical and the analytical solutions. The AT2 and PCM models are both used in the analysis. The force–displacement diagram in Fig. 9(a) presents the relation between the horizontal resultant force $F_{x_1}$ and the horizontal displacement $\bar{u}_1$ at the left edge. The numerical solutions compare well with the analytical solutions. The force–displacement diagram shows a softening response, as expected considering the use of the Xu–Needleman law. Due to the localisation property of the PCM model, the error of the force in the case of the PCM model is smaller than that for the AT2 model, see Fig. 9(b). Fig. 10(a) presents the stress along the centre plane $x_2 = 0.5$. A slight discrepancy is observed, since the error for the AT2 model is bigger than that for the PCM model, see Fig. 10(b). This is due to the larger support in the AT2 model, see Fig. 3. In fact, the discrepancy in the stress is a direct consequence of the mismatch in the approximation orders of the two strain contributions in Eq. (28) [11]. This can be remedied by employing different approximation orders of the displacement and the displacement jump [11,14].

### 6.2. L-shaped plate peeling test

Next, the L-shaped beam of Fig. 11(a) is considered. Roller boundary conditions are employed and the beam is loaded in the horizontal as well as in the vertical direction, by gradually increasing the displacement $\bar{u}$ of the bottom and left edges. Linear isotropic elasticity is used to describe the bulk material, with a Young's modulus $E = 250$ MPa and a Poisson's ratio $\nu = 0.2$. Plane-strain conditions have been assumed. The interface $\Gamma_c$ is indicated by a solid line along the diagonal of the beam. A Xu–Needleman cohesive zone model has again been employed to describe the debonding of the interface with $t_u = 1$ MPa and $\mathcal{G}_c = 0.1$ N/mm. The penetration stiffness is set as $k_p = 1 \times 10^5$ MPa/mm to prevent the interpenetration. We have used the PCM model to construct the phase field and the Dirac-delta function in the proposed phase field model.

The response curves under different loading steps are shown in Figs. 11(b). A discrete interface model has been used to provide the reference solution [38]. The figure shows that the results of the proposed method are in a good agreement with the reference solution. Fig. 12 shows the radial displacement and radial stress distribution under $\bar{u} =$

0.4 mm. The displacement and stress distribution again match well. For the proposed method, there are oscillations in the displacement and stress plot around the smeared interface $\Gamma_\xi$ due to the regularisation. We observe a clear displacement jump along the interface $\Gamma_c$.

### 6.3. Fibre–epoxy debonding test

A problem of fibre–epoxy debonding is analysed by a two-dimensional model assuming plane-strain conditions [38]. The geometry of the specimen is shown in Fig. 13(a). Due to symmetry, only one quarter of the specimen has been considered with symmetry-enforcing boundary conditions. The material properties are as follows. For the fibre Young's modulus $E = 225$ GPa and Poisson's ratio $\nu = 0.2$, and for the epoxy we have a Young's modulus $E = 4.3$ GPa and a Poisson's ratio $\nu = 0.34$. The tractions at the fibre–epoxy interface have again been assumed to follow the Xu–Needleman relation with $t_u = 50$ MPa and $\mathcal{G}_c = 4 \times 10^{-3}$ N/mm. To prevent interpenetration, a penetration stiffness has been added with $k_p = 10^5$ MPa/mm. The PCM model is used to build the phase field.

The response curve is presented in terms of the horizontal stress $\sigma_1$ as a function of the prescribed displacement $\bar{u}$, see Fig. 13(b). The results agree well with the solution of the discrete interface model [38]. The displacement, and the stress of fibre and epoxy are illustrated in Fig. 14. The results of the proposed method again compare well with those of the discrete interface model. There are oscillations in the plot around the smeared interface $\Gamma_\xi$. The plot shows obvious displacement jump along the interface $\Gamma_c$. In this example we could have included failure in the matrix by introducing the surface energy function [25–27]. Then, both cohesive cracking for the interface and subsequent kinking of the primary crack into the matrix can be simulated. This has not been pursued since in the current study the focus is on the phase-field regularised cohesive zone model for the interface.

## 7. Concluding remarks

Phase field model can be employed in cohesive interface modelling. In the present approach, the discrete interface is regularised in a smeared sense, avoiding topological changes. The displacement jump of the interface is modelled explicitly, in addition to the displacement field, thus avoiding the need for enrichment functions as in the extended finite element method (XFEM). The cohesive zone law from the discrete model is directly employed in the analysis, avoiding the modification of degradation function used before in the phase field method. We have examined three different forms of the regularised function. For the Dirac-delta function is approximated by an exponential function, the support of the smeared interface is spread over the entire domain. Especially for modelling an interface, this is less suitable and regularisations which employ a compact support are more accurate. A difficulty resides in the numerical implementation since imposing the phase field in the domain is non-trivial due to the boundary condition imposition. Here, the use of analytical solutions of the phase field leads to more accurate results.

Starting from the variational form of the energy functional, we can arrive at the exact strain of the regularised extended finite element method. To satisfy the property of Dirac-delta function, the displacement jump should be constant in the normal direction, which is enforced by a penalty term in the energy functional. Due to this requirement, we should prescribe the displacement jump degrees of freedom in the entire domain, similar to the displacement degrees of freedom. For the aforementioned phase field approximations with a compact support the Dirac-delta function will be zero outside the smeared interface, automatically guaranteeing the strong form of the traction equation.

## CRediT authorship contribution statement

**L. Chen:** Modified the original version of the cohesive phase-field model with a discrete jump to a regularised, smeared version, implemented the method, run the examples and made the first draft of the paper. **R. de Borst:** One of the developers of the aforementioned original version and has finalised the paper.

## Declaration of competing interest

The authors declare that they have no known competing financial interests or personal relationships that could have appeared to influence the work reported in this paper.

## Data availability

No data was used for the research described in the article.

## Acknowledgement

Financial support from the European Research Council (Advanced Grant 664734 "PoroFrac") is gratefully acknowledged.

## References

[1] D. Ngo, A.C. Scordelis, Finite element analysis of reinforced concrete beams, J. Am. Concrete Inst. 64 (1967) 152–163.
[2] Y.R. Rashid, Analysis of reinforced concrete pressure vessels, Nucl. Eng. Des. 7 (1968) 334–344.
[3] R. de Borst, Some recent issues in computational failure mechanics, Internat. J. Numer. Methods Engrg. 52 (2001) 63–95.
[4] R. de Borst, M.A. Gutiérrez, A unified framework for concrete damage and fracture models including size effects, Int. J. Fract. 95 (1999) 261–277.
[5] G.A. Francfort, J.J. Marigo, Revisiting brittle fracture as an energy minimization problem, J. Mech. Phys. Solids 46 (1998) 1319–1342.
[6] B. Bourdin, G.A. Francfort, J.J. Marigo, The variational approach to fracture, J. Elasticity 91 (2008) 5–148.
[7] C. Miehe, M. Hofacker, F. Welschinger, A phase field model for rate-independent crack propagation: Robust algorithmic implementation based on operator splits, Comput. Methods Appl. Mech. Engrg. 199 (2010) 2765–2778.
[8] C. Miehe, F. Welschinger, M. Hofacker, Thermodynamically consistent phase-field models of fracture: Variational principles and multi-field FE implementations, Internat. J. Numer. Methods Engrg. 83 (2010) 1273–1311.
[9] B. Bourdin, G.A. Francfort, J.J. Marigo, Numerical experiments in revisited brittle fracture, J. Mech. Phys. Solids 48 (2000) 797–826.
[10] M.J. Borden, C.V. Verhoosel, M.A. Scott, T.J.R. Hughes, C.M. Landis, A phase-field description of dynamic brittle fracture, Comput. Methods Appl. Mech. Engrg. 217–220 (2012) 77–95.
[11] C.V. Verhoosel, R. de Borst, A phase-field model for cohesive fracture, Internat. J. Numer. Methods Engrg. 96 (2013) 43–62.
[12] J. Vignollet, S. May, R. de Borst, C.V. Verhoosel, Phase-field models for brittle and cohesive fracture, Meccanica 49 (2014) 2587–2601.
[13] S. May, J. Vignollet, R. de Borst, A numerical assessment of phase-field models for brittle and cohesive fracture: $\Gamma$-convergence and stress oscillations, Eur. J. Mech. A Solids 52 (2015) 72–84.
[14] Y. Ghaffari Motlagh, R. de Borst, Considerations on a phase-field model for adhesive fracture, Internat. J. Numer. Methods Engrg. 121 (2020) 2946–2963.
[15] T.-T. Nguyen, J. Yvonnet, Q.-Z. Zhu, M. Bornert, C. Chateau, A phase-field method for computational modeling of interfacial damage interacting with crack propagation in realistic microstructures obtained by microtomography, Comput. Methods Appl. Mech. Engrg. 312 (2016) 567–595.
[16] S. Conti, M. Focardi, F. Iurlano, Phase field approximation of cohesive fracture models, Ann. Inst. Henri Poincare C 33 (2016) 1033–1067.
[17] J.Y. Wu, A unified phase-field theory for the mechanics of damage and quasi-brittle failure, J. Mech. Phys. Solids 103 (2017) 72–99.
[18] L. Chen, R. de Borst, Phase-field modelling of cohesive fracture, Eur. J. Mech. A Solids 90 (2021) 104343.
[19] C. Chukwudozie, B. Bourdin, K. Yoshioka, A variational phase-field model for hydraulic fracturing in porous media, Comput. Methods Appl. Mech. Engrg. 347 (2019) 957–982.
[20] K. Yoshioka, D. Naumov, O. Kolditz, On crack opening computation in variational phase-field models for fracture, Comput. Methods Appl. Mech. Engrg. 369 (2020) 113210.
[21] D.S. Dugdale, Yielding of steel sheets containing slits, J. Mech. Phys. Solids 8 (1960) 100–104.

[22] G.I. Barenblatt, The mathematical theory of equilibrium cracks in brittle fracture, Adv. Appl. Mech. 7 (1962) 55–129.
[23] X.P. Xu, A. Needleman, Void nucleation by inclusion debonding in a crystal matrix, Modelling Simulation Mater. Sci. Eng. 1 (1993) 111–132.
[24] J.J.C. Remmers, R. de Borst, A. Needleman, The simulation of dynamic crack propagation using the cohesive segments method, J. Mech. Phys. Solids 56 (2008) 70–92.
[25] M. Paggi, J. Reinoso, Revisiting the problem of a crack impinging on an interface: A modeling framework for the interaction between the phase field approach for brittle fracture and the interface cohesive zone model, Comput. Methods Appl. Mech. Engrg. 321 (2017) 145–172.
[26] D. Pranavi, A. Rajagopal, J.N. Reddy, Interaction of anisotropic crack phase field with interface cohesive zone model for fiber reinforced composites, Compos. Struct. 270 (2021) 114038.
[27] G. Li, B.B. Yin, L.W. Zhang, K.M. Liew, Modeling microfracture evolution in heterogeneous composites: A coupled cohesive phase-field model, J. Mech. Phys. Solids 142 (2020) 103968.
[28] K. Park, G.H. Paulino, Cohesive zone models: A critical review of traction-separation relationships across fracture surfaces, Appl. Mech. Rev. 64 (2011) 060802.
[29] L. Chen, R. de Borst, Cohesive fracture analysis using Powell-Sabin B-splines, Int. J. Numer. Anal. Methods Geomech. 43 (2019) 625–640.
[30] L. Ambrosio, V.M. Tortorelli, Approximation of functional depending on jumps by elliptic functional via t-convergence, Comm. Pure Appl. Math. 43 (1990) 999–1036.
[31] F. Fathi, L. Chen, R. de Borst, Extended isogeometric analysis for cohesive fracture, Internat. J. Numer. Methods Engrg. 121 (2020) 4584–4613.
[32] F. Fathi, L. Chen, R. de Borst, X-IGALME: Isogeometric analysis extended with local maximum entropy for fracture analysis, Internat. J. Numer. Methods Engrg. 122 (2021) 6103–6125.
[33] L. Chen, R. de Borst, Cohesive fracture analysis using Powell-Sabin B-splines, Int. J. Numer. Anal. Methods Geomech. 43 (2019) 625–640.
[34] L. Chen, B. Li, R. de Borst, The use of Powell-Sabin B-splines in a higher-order phase-field model for crack kinking, Comput. Mech. 67 (2021) 127–137.
[35] C. Geuzaine, J.-F. Remacle, Gmsh: A 3-D finite element mesh generator with built-in pre-and post-processing facilities, Internat. J. Numer. Methods Engrg. 79 (2009) 1309–1331.
[36] L. Chen, B. Li, R. de Borst, Energy conservation during remeshing in the analysis of dynamic fracture, Internat. J. Numer. Methods Engrg. 120 (2019) 433–446.
[37] T. Sorokina, A.J. Worsey, A multivariate Powell–Sabin interpolant, Adv. Comput. Math. 29 (2008) 71–89.
[38] L. Chen, F.J. Lingen, R. de Borst, Adaptive hierarchical refinement of NURBS in cohesive fracture analysis, Internat. J. Numer. Methods Engrg. 112 (2017) 2151–2173.